ACS APPLIED MATERIALS & INTERFACES

Research Article

www.acsami.org

Controllable Synthesis, Magnetic Properties, and Enhanced Photocatalytic Activity of Spindlelike Mesoporous α-Fe_2O_3/ZnO Core–Shell Heterostructures

Wei Wu,*[,†,‡] Shaofeng Zhang,[‡,§] Xiangheng Xiao,[‡,§] Juan Zhou,[‡,§] Feng Ren,[‡,§] Lingling Sun,[‡,§] and Changzhong Jiang*[,‡,§]

[†]School of Printing and Packaging and School of Chemistry and Molecular Science, [‡]Key Laboratory of Artificial Micro- and Nano-structures of Ministry of Education, [§]Center for Electronic Microscopy and School of Physics and Technology, Wuhan University, Wuhan 430072, P. R. China

Supporting Information

ABSTRACT: Mesoporous spindlelike iron oxide/ZnO core–shell heterostructures are successfully fabricated by a low-cost, surfactant-free, and environmentally friendly seed-mediate strategy with the help of postannealing treatment. The material composition and stoichiometry, as well as these magnetic and optical properties, have been examined and verified by means of high-resolution transmission electron microscopy and X-ray diffraction, the thickness of ZnO layer can be simply tailored by the concentration of zinc precursor. Considering that both α-Fe_2O_3 and ZnO are good photocatalytic materials, we have investigated the photodegradation performances of the core–shell heterostructures using organic dyes Rhodamin B (RhB). It is interesting to find that the as-obtained iron oxides/ZnO core–shell heterostructures exhibited enhanced visible light or UV photocatalytic abilities, remarkably superior to the as-used α-Fe_2O_3 seeds and commercial TiO_2 products (P25), mainly owing to the synergistic effect between the narrow and wide bandgap semiconductors and effective electron–hole separation at the interfaces of iron oxides/ZnO.

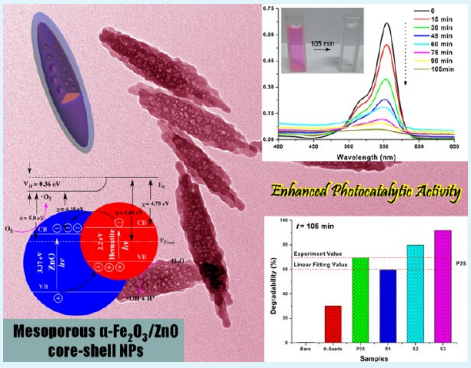

KEYWORDS: *mesoporous structure, heterostructure, magnetic properties, photocatalyst, semiconductors*

INTRODUCTION

Multicomponent core–shell heterostructures exhibit promising magnetic, optical, and catalytic properties, quite distinct from those of their single counterparts.[1] These advantages make core–shell heterostructures become one of the most promising candidates for the exploration of new applications and practical significance for many different disciplines. The physical and chemical properties of core–shell heterostructures are determined and limited not only by their chemical composition but also by the distribution of their physical dimensions, structure, core–shell shape, and size.

According to the thermodynamic requirement of photocatalytic reaction, the redox potential of the valence band (VB) hole must be sufficiently positive to generate hydroxyl radicals and that of the conduction band (CB) electron must be sufficiently negative to generate superoxide radicals.[2] Therefore, it has been reported that ZnO can also be used as a major component of photocatalyst due to its similar bandgap energy (3.2 eV) and favorable band gap positions compared to the other materials.[3] However, there are two bottleneck drawbacks associated with semiconductor photocatalysts currently, namely, high charge recombination rate inherently and low efficiency for utilizing solar light, which would greatly hinder the commercialization of this technology.[4] Therefore, various methods have been developed to reduce the recombination rate of photogenerated electrons and holes or increase the utilizing rate of visible light in ZnO-based photocatalysts. More importantly, traditional charge transfer between the narrow and wide bandgap semiconductors is beneficial to isolate the oxidation reaction due to the holes, and the reduction reaction due to the electrons at two different sites, in order to prevent the charge-carrier recombination. Moreover, the incorporation of small band gap semiconductors, dyes and cocatalysts, increases the probability of absorption of radiation in the visible range. For example, we successfully prepared iron oxide/SnO_2 and iron oxide/TiO_2 core–shell photocatalysts by hydrothermal method in recently, the results reveal that the combination of narrow bandgap (α-Fe_2O_3, 2.2 eV) and wide bandgap semiconductors will enhanced their photocatalysis abilities.[5,6]

More recently, Chiu et al have synthesized spherical Fe_3O_4/ZnO core/shell nanocrystals by seed-mediated growth approach in nonhydrolytic condition.[7] Chen and co-workers have fabricated Fe_3O_4/ZnO core/shell nanorods by combing

Received: April 16, 2012
Accepted: June 12, 2012
Published: June 12, 2012

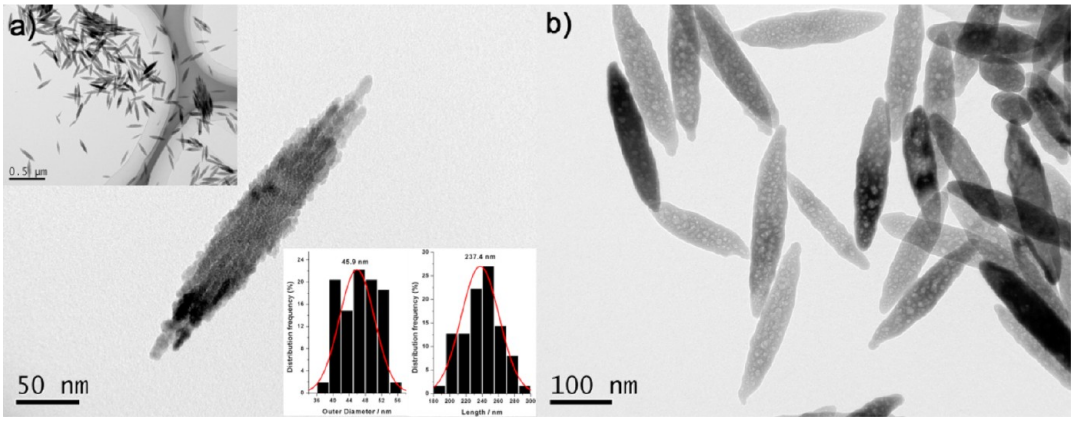

Figure 1. TEM images of (a) a single hematite seed (the inset at left top corner is the overall feature of hematite seeds at low-magnification, the inset at right corner is the corresponding size histograms for the length and outer diameter of hematite seeds) and (b) the hematite seeds after annealing treatment.

an inorganic-phase reaction with a hydrogen annealing process, and the results reveal that the composite nanorods is a kind of electromagnetic wave adsorptive materials.[8] Herein, we successfully prepared the spindle-like mesoporous α-Fe_2O_3/ZnO core–shell heterostructures with high purity based on α-Fe_2O_3 nanospindles by a facile wet-chemical routes and subsequent annealing treatment. The different structure features of the iron oxide/ZnO composite particles can be obtained by adjusting the used amount of zinc ions concentration, and the as-prepared samples were investigated by TEM aiming to explore the formation mechanism, which would provide us some insights into the elaborate structure architecting and functionality tailoring for the core–shell heterostructures. Moreover, investigations on the photodegradability of the naked iron oxide seeds, commercial TiO_2 nanoparticles (P25) and as-synthesized α-Fe_2O_3/ZnO core–shell heterostructures for RhB dyes were performed to compare their photocatalytic activities.

EXPERIMENT DETAILS

Materials. Zinc acetate dihydrate ($Zn(Ac)_2{\cdot}2H_2O$, Ac = CH_3COO), potassium hydroxide (KOH), Ethanol (95%), ammonia ($NH_3{\cdot}H_2O$), Ferric chloride hexahydrate ($FeCl_3{\cdot}6H_2O$), sodium dihydrogen phosphate dihydrate ($NaH_2PO_4{\cdot}2H_2O$) were purchased from Sinopharm Chemical Reagent CO., Ltd., RhB dyes were purchased from Aladdin Chemical Reagent Co., Ltd., Degussa P25, which contains 80% anatase crystallites and 20% rutile crystallites with an average particle size of 30 nm and a BET surface area of ~50 m^2/g, was obtained from Degussa AG (Germany). All chemicals were analytical grade (AR) and used as received without purification.

Synthesis of Iron Oxide/ZnO Composite Particles. The composites were fabricated via a three-step process: (1) α-Fe_2O_3 seeds were fabricated and the detail synthesis process was described in our previous report by a forced hydrolysis method.[9] Briefly, 100 mL of 4.5×10^{-4} M NaH_2PO_4 solution was transferred to a flask and heated to 95 °C. Then 1.8 mL of 1.48 M $FeCl_3$ solution was added dropwise into the flask, and the mixture was aged at 100 °C for 14 h. After the resulting mixture was cooled down to room temperature naturally, the product was centrifuged and washed with double distilled water and ethanol. (2) α-Fe_2O_3/ZnO core–shell composites were synthesized by a seed-mediate method. Typically, 20 mL of above α-Fe_2O_3 seeds (8 mg/mL) was dispersed in 130 mL of water by ultrasonication disperse. Then 50 mL of a certain concentration of $Zn(Ac)_2$ were dropped into the above solvent at the stirring rate of 500 rpm. Subsequently, 20 mL of 5 wt % ammonia solution was dropped added into the flask when the reaction temperature elevated to 40 °C, and the resulting solution was further allowed to react for 1 h. The resulting solution was further collected by centrifugation at 10000 rpm for 10 min. (3) Finally, the precipitates were annealed at 550 °C for 2 h in air atmosphere with the heating rate of 10 °C/min. The obtained samples at different concentration of zinc precursor ($C_{Zn\ ions}$) of 0.02, 0.04, and 0.08 M were named S1, S2, and S3, respectively.

Photodegradation Measurement. First, 100 mL of RhB solution with a concentration of 6 mg/L was prepared. As-prepared samples were weighed (20 mg) and added to 40 mL of the above RhB solutions, respectively. The suspension was stirred in the dark for 30 min in order to reach absorption equilibrium. And then the mixed solutions were illuminated under mercury and tungsten mixed light lamp (OSRAM, 250W, including UV and visible light), and the RhB solutions were illuminated under light in the photochemical reactor. The solutions were fetched at 15 min intervals by pipet for each solution and centrifuged. UV–vis adsorption spectra were recorded at different intervals to monitor the degradation process using a Shimadzu 2450/2550PC spectrophotometer.

Characterization. Powder X-ray diffraction (XRD) patterns of the samples were recorded on a D8 Advance X-ray diffractometer (Germany) using Cu Kα radiation (λ = 0.1542 nm) operated at 40 kV and 40 mA and at a scan rate of 0.05° 2θ s^{-1}. Transmission electron microscopy (TEM) images and selected area electron diffraction (SAED) patterns were performed with a JEOL JEM-2010 (HT) transmission electron microscope at the accelerating voltage of 200 kV, and all the samples dissolved in ethanol by ultrasonic treatment (5 min) and dropped on copper grids. High-resolution transmission electron microscopy (HRTEM) images were performed on a JEOL JEM-2010 FEF (UHR) transmission electron microscope at the accelerating voltage of 200 kV equipped with energy dispersive X-ray spectrometer (EDX), and the samples also dissolved in ethanol and dropped on carbon covered copper grids. Magnetic measurements were performed on a Quantum Design MPMS XL-7 SQUID magnetometer. The powder sample was filled in a diamagnetic plastic capsule, and the packed sample was then put in a diamagnetic plastic straw and impacted into a minimal volume for magnetic measurements. Background magnetic measurements were checked for the packing material.

RESULTS AND DISCUSSION

Figure 1a shows the TEM image of as-used single α-Fe_2O_3 seed, and the insert image illustrates that large-scale α-Fe_2O_3 with a uniform size. The average length and outer diameter of these hematite seeds are 232.4 and 42.9 nm, respectively. (The result was statistically analyzed by JEOL SmileView software, with more than 100 resoluble spindle-like particles). Figure 1b depicts the TEM images of α-Fe_2O_3 seeds after annealing treatment. It can be clearly seen that the shape and size of the particles are well preserved. It is noteworthy that the spindle-

dx.doi.org/10.1021/am300669a | ACS Appl. Mater. Interfaces 2012, 4, 3602–3609

like particles present mesoporous morphology. The porous size is ca. 5−8 nm and the recrystallization results in the formation of mesoporous hematite. The origin of these pores can be assigned to the dehydroxylation of β-FeOOH to form α-Fe_2O_3.[10] Moreover, the structure and phase purity of the as-obtained products were examined by PXRD, as shown in curve a in Figure S1 (see the Supporting Information), and all of the peaks can be well indexed to a pure rhombohedral structure with an *R*3*c* space group for hematite (JCPDS PDF 33−0664).[11] α-Fe_2O_3 is extremely stable and is often the end number of transformations of other iron oxides. The crystal phase will not change in the current annealing temperature, and the result have been present in curve b in Figure S1 in the Supporting Information.

The crystallinity, phase, and purity of the samples of α-Fe_2O_3 after ZnO coating were determined by XRD. Figure 2 shows

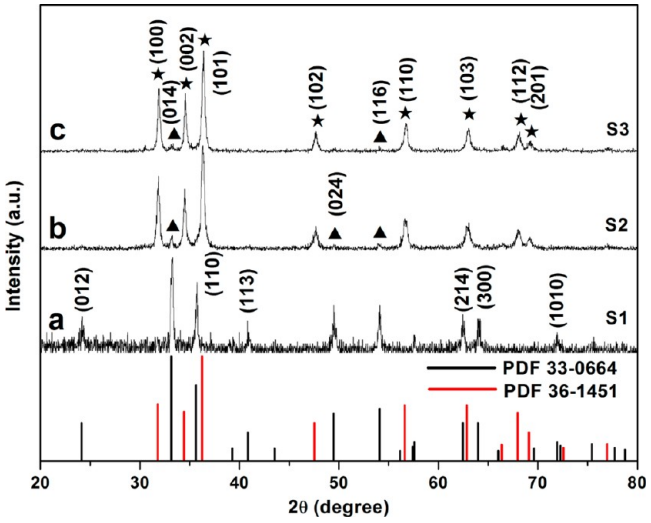

Figure 2. XRD patterns of three α-Fe_2O_3/ZnO core−shell heterostructures: S1, S2, and S3. The standard XRD patterns of α-Fe_2O_3 and ZnO, drawn from the respective JCPDF files, are shown at the bottom in black and red, respectively.

the XRD patterns of the samples with different concentration of zinc precursor. XRD peaks of the S1 (curve a, $C_{Zn\ ions}$ = 0. 02 M) represent the rhombohedral corundum phase of α-Fe_2O_3 with lattice parameters a = 5.0357 Å and c = 13.7489 Å, matching well with the JCPDS card #33−0664 corresponding to the powder diffraction pattern of standard hematite. The ZnO peaks cannot be clearly identified, the possible reasons are the ZnO with low degree of crystallinity and very low proportion in samples. In the following section, the ZnO layer was confirmed by HRTEM and EDX analysis. By increasing the Zn ions concentration, the ZnO peaks can be clear identified in S2 (curve b, $C_{Zn\ ions}$ = 0.04 M) and S3 (curve c, $C_{Zn\ ions}$ = 0.08 M), both of the patterns of these single-constituents can be well indexed to the standard patterns of ZnO (PDF 36−1451, hexagonal phase) and α-Fe_2O_3 (PDF 33−0664, rhombohedral phase), respectively. The current results suggest that the shell growths for both S2 and S3 yield a crystalline shell without alloying, because it has been confirmed that homogeneous alloying can cause obvious shifts in the diffraction patterns.[12,13]

Subsequently, the morphology feature of the as-prepared mesoporous iron oxide/ZnO sample (S2, $C_{Zn\ ions}$ = 0.04 M) was detailed investigated by TEM, and shown in Figure 3. Figure 3a shows the low-magnification TEM micrograph for the as-prepared hematite/ZnO composite nanoparticles, and all the particles are spindle-like in shape with an average diameter of 49.5 nm and a length of 240.2 nm. Additionally, there are no clear agglomerations observed between two particles. The bright ring patterns from SAED of the sample given in Figure 3a can be well-indexed to the hexagonal crystalline phase of hematite and ZnO aggregates. As shown in Figure 3b, a close observation of hematite/ZnO composite particles clearly shows the formation of uniform spindlelike core−shell structure. The α-Fe_2O_3 mesoporous core appears black and ZnO shell is light colored in the image because hematite has a higher mass−thickness contrast. The average thickness of the ZnO shell is observed to be ca. 10 nm according to the difference in contrast between the core and shell regime. The mesoporous structure of S2 have also been confirmed by nitrogen adsorption−desorption isotherms (see Figure S2 in the Supporting Information), and the sample exhibits a type H3 hysteresis loop according to Brunauer−Deming−Deming−Teller (BDDT) classification, which indicated the presence of mesopores (2−50 nm) with a cylindrical pore mode. Figure 3d is the dark field micrograph of Figure 3c by setting Z (002) ring of ZnO (see the SAED in Figure 3a), thus the ZnO shell layer are imaged as brighter dots. Combining with the XRD and SAED results, the above observation results demonstrate that α-Fe_2O_3/ZnO core−shell particles are successfully fabricated by our method.

In order to better investigate the crystal structure of the spindle-like α-Fe_2O_3/ZnO composite particles, HRTEM and in situ EDX patterns of as-obtained sample S2 were performed and are shown in Figure 4. A close observation of a single α-Fe_2O_3/ZnO particle clearly shows the formation of core−shell structure (Figure 4a). The α-Fe_2O_3 core appears black and the ZnO shell is light colored in the image because hematite has a higher mass−thickness contrast. The HRTEM image shows alternate bright and dark regions that signify the variations in the surface thickness in the hematite core. The results illustrate the core with mesoporous structures have been formed in the annealing process. We carried out the EDX analysis in different regions of this composite particle. The tip regions (1# and 3#) of composite particle showed a very high atomic ratio of Zn to Fe. This ratio decreased in the 2# region far away from the tip regions, the results reveals that the ZnO have been successfully coated on the surface of α-Fe_2O_3 seeds. As shown in Figure 4b, the interplanar spacings of 0.282 and 0.270 nm obtained by HRTEM can be indexed to the (100) plane of ZnO and (104) plane of α-Fe_2O_3, respectively. From the Fourier transformation (FFT) pattern (insert in Figure 4b), it can be concluded that the iron oxide follows the hexagonal closed pack corundum structure with the layer stacked along the [001] direction (*c* axis). Those results reveal that α-Fe_2O_3/ZnO core−shell structures are successfully fabricated by the present method.

For further investigating the growth mechanism of spindle-like mesoporous α-Fe_2O_3/ZnO core−shell particles, we decrease and increase the concentration of zinc ions to α-Fe_2O_3 seeds, respectively, and the TEM micrographs of as-obtained products S1 and S3 are shown in Figure 5. When the reaction was conducted at $C_{Zn\ ions}$ = 0.02 M, the SEM image (Figure 5a) shows uniform spindle structure, and the insert EDX spectrum reveals that the sample compositions contain Zn, Fe and O elements. The TEM and HRTEM images in Figure 5b,c provide further insight into the morphology and

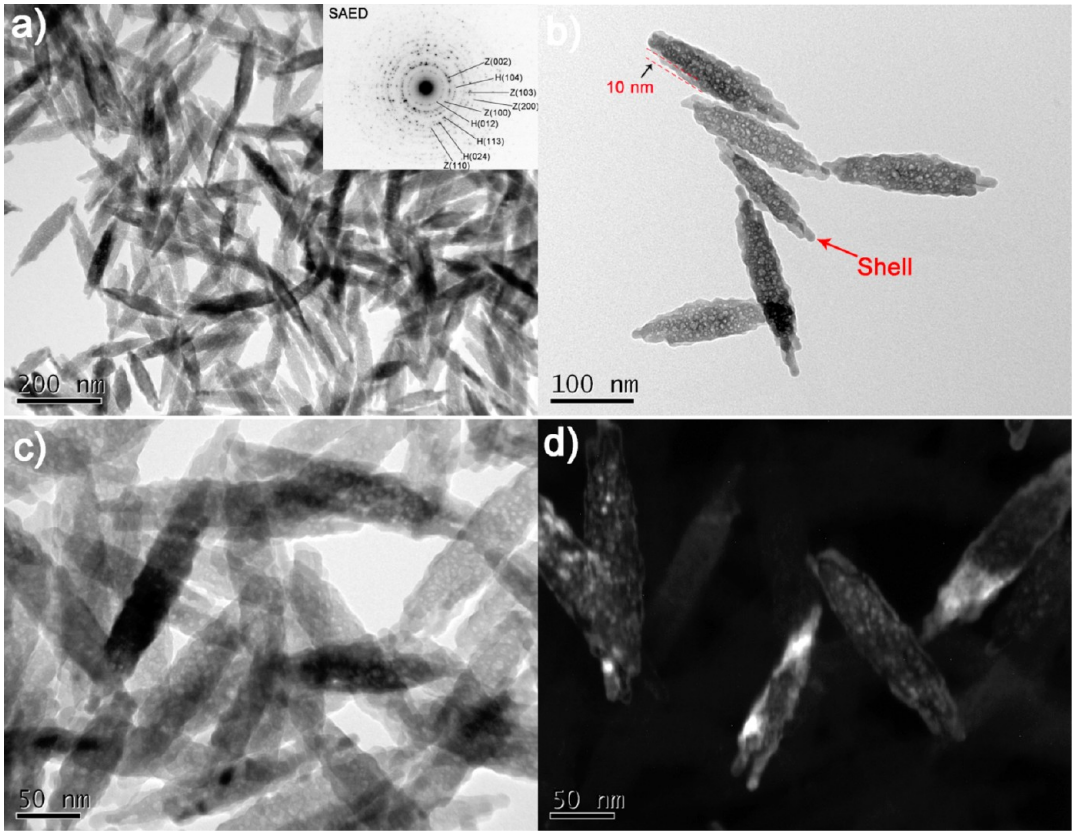

Figure 3. (a) Low-magnification bright-field TEM image and the insert is the SAED patterns; (b) a high-magnification bright-field TEM image; the (c) bright-field and (d) corresponding dark-field TEM images of the α-Fe_2O_3/ZnO core−shell heterostructures (S2).

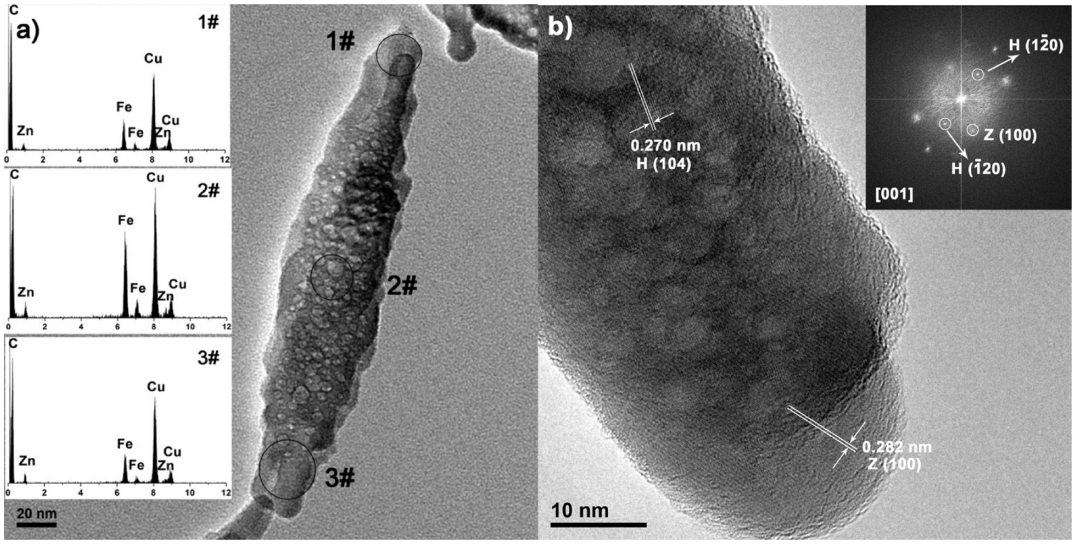

Figure 4. (a) EDX patterns from different regions and (b) HRTEM image of single α-Fe_2O_3/ZnO core−shell heterostructure (the inset is the corresponding FFT image).

surface properties of the prepared sample S1. A close observation of a single particle clearly shows the formation of core−shell structure. The core thickness of S1 is ca. 7 nm and the core regions display a clear mesoporous nature. And the HRTEM image (insert in Figure 5c) of the tip region shows the lattice planes with interplanar spacing of 0.281 nm corresponding to the (100) plane of ZnO. When the Zn ions concentration of precursor elevated to 0.08 M, the sample S3 presents the spindle or somatoid shapes, as shown in images d and e in Figure 5. By close comparison, one can see that the tips of the S3 are not so speculate as those of the pristine α-Fe_2O_3 seeds and previous samples S1 and S2 (Figure 5f), the result illustrates that two or more α-Fe_2O_3 seeds were packed in a single composite particle. Compare with the S1, the composite particle showed a very high atomic ratio of Zn to Fe in EDX spectrum. The difference may be related to the large excess of ZnO coating, which can be further proved by the insert HRTEM image in Figure 5f, and a lattice spacing of 0.191

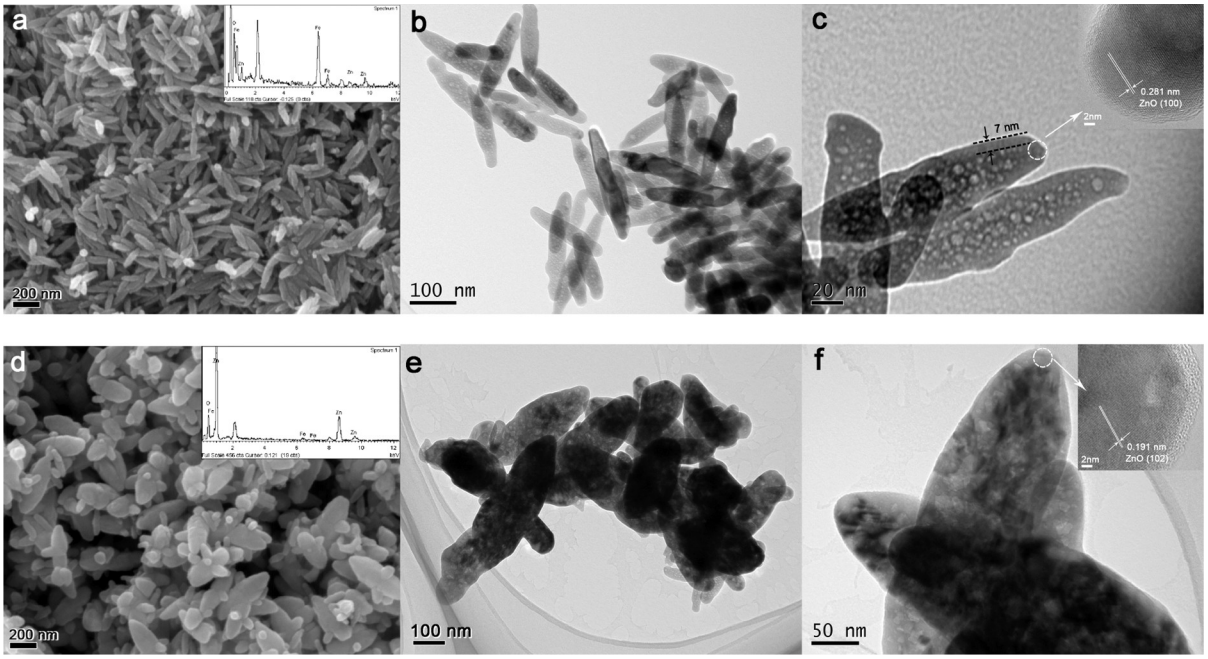

Figure 5. Typical FESEM, EDX, TEM, and HRTEM images for (a–c) sample S1 ($C_{Zn\ ions}$ = 0.02 M) and (d–f) S3 ($C_{Zn\ ions}$ = 0.08 M), respectively.

nm for the (102) plane of ZnO shell can be observed on the surface of S3. The above results reveal that the ZnO shell thickness can be tailored by the Zn ions concentration in the precursor, and excess Zn ions concentration is not beneficial to maintain the morphology and shape of original α-Fe_2O_3 seeds.

The synthetic route and formation mechanism for fabricating the mesoporous hematite/ZnO core–shell heterostructures was shown in Scheme 1, in seed-mediated growth method, the shell formation involves two steps, mainly concluding the adsorption on the surface of monodisperse seeds and the growth under annealing treatment. Due to the presence of spindle-like hematite seeds, the growth of ZnO shell proceeded through heterogeneous nucleation rather than forming separate nuclei by homogeneous nucleation. Figure S3 in the Supporting Information shows the HRTEM image of a single α-Fe_2O_3 seed, a large number of gaps are distributed between both grain boundaries, and the result reveals that the spindle-like particle is composed of small nanocrystals and the overall surface of the particle is rough. This feature endows the α-Fe_2O_3 seeds with high adsorption for the zinc ions. The adsorbed zinc precursor would react with ammonia and form $Zn(OH)_2$. In the annealing process with a slow heating rate, the $Zn(OH)_2$ decompose and form ZnO shell layer on the surface of α-Fe_2O_3 seeds and finally generating core–shell nanostructures ($Zn^{2+} + 2OH^- \rightarrow Zn(OH)_2 \xrightarrow{\Delta} ZnO + H_2O$).[14] Additionally, the mesoporous core has been observed due to the dehydroxylation of β-FeOOH to form α-Fe_2O_3 in annealing process.

Scheme 1. Synthetic Route and Formation Mechanism for Fabricating the Mesoporous Hematite–ZnO Core–shell Composite Particles[a]

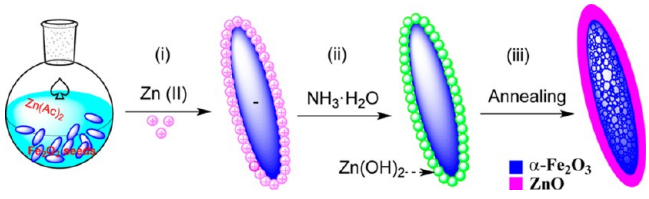

[a](i) The zinc precursor absorbed on the surface and small gaps of hematite seeds; (ii) adding ammonia to $Zn(Ac)_2$ causes an instant supersaturation of $[Zn(OH)_4]_2^-$ (growth units) and forms $Zn(OH)_2$ on the surface of hematite seeds because of the enhanced concentration of OH^- ions; (iii) the $Zn(OH)_2$ decomposes and forms ZnO coating layer because of the annealing treatment, and hematite seeds will form as mesoporous structures.

Moreover, the room-temperature magnetic properties of the spindle-like α-Fe_2O_3 seeds and α-Fe_2O_3/ZnO core–shell particles were investigated by SQUID. As shown in Figure 6a, the saturation magnetization (M_S) of α-Fe_2O_3 seeds is 0.64 emu g^{-1}. After coating, the M_S values of α-Fe_2O_3/ZnO decrease to 0.43, 0.029, and 0.0098 emu g^{-1} for S1, S2, and S3, respectively. As a result of the interaction with the ligands or outer layers like the ZnO coating, indicating that the surface anisotropy probably also affects the moment of the inner iron oxide nanoparticles via the exchange interaction with those at the surface.[15–17] Thus, the M_S of iron oxide nanoparticles was decreased by the immobilization of the ZnO shell on their surfaces. The α-Fe_2O_3/ZnO samples have a negligible remanent magnetization (M_R) characters, and all samples exhibits soft magnetic properties and their coercivity values are very low. It is noteworthy that the S3 displays a clear antiferromagnetic property (Figure 6b), the result reveals that the increasing of ZnO thickness will induce the disorder structure of hematite cores, the nonsaturation of moments at high field represents the contribution of the α-Fe_2O_3 antiferromagnetic core,[18,19] and this is also an interesting ferromagnetic-antiferromagnetic transition behavior.

The photocatalytic activity was examined by a colorant decomposition test using RhB dyes. The RhB displays an absorption peak at the wavelength of about 554 nm in the absorption spectra. Panels a and b in Figure 7 show the typical time evolution of absorption spectra of RhB after photodegradation with the sample S1 and S3. With time increasing,

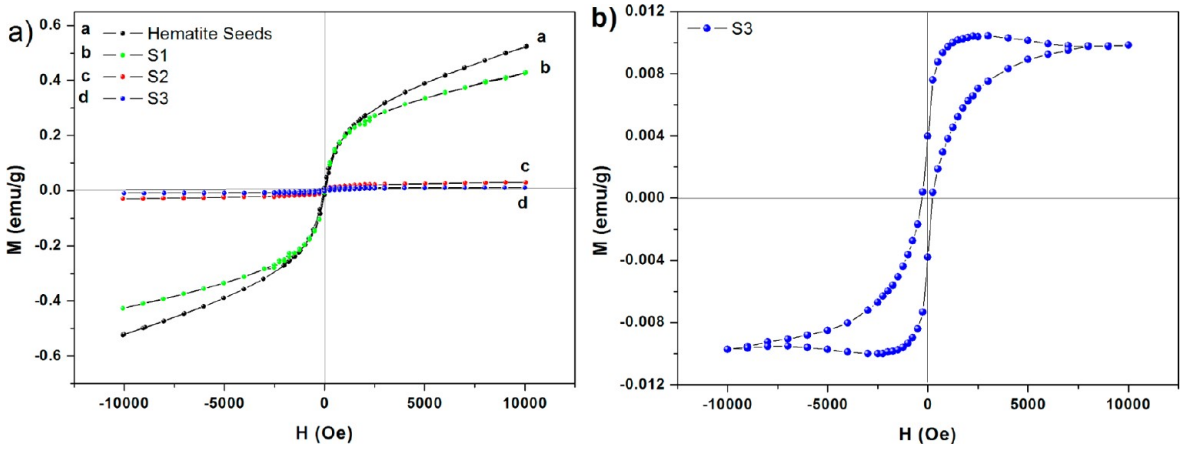

Figure 6. (a) Hysteresis curves of hematite seeds and samples S1, S2, and S3, and (b) the magnified hysteresis loops of S3.

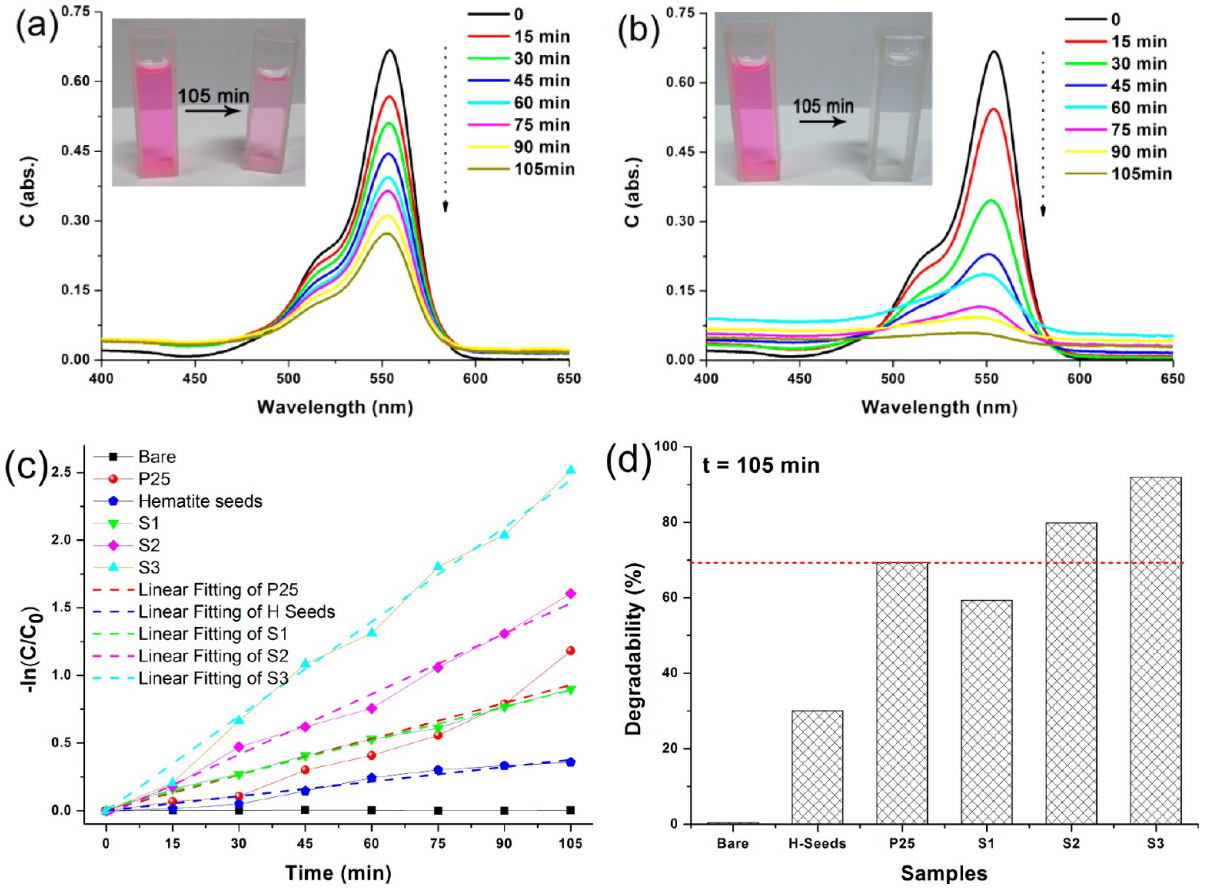

Figure 7. Absorption spectra of the RhB solution as a function of UV irradiation time in the presence of (a) S1 and (b) S3; the insets in the left-top corners are the photographs of color change of RhB solution before and after photodegradation; (c) logarithm of the normalized concentrations as a function of UV irradiation time for the RhB solution containing various photocatalysts: bare (■), P25 TiO_2 (●), α-Fe_2O_3 (★), S1 (▼), S2 (♦), and S3 (▲); (d) RhB degradabilities of α-Fe_2O_3 seeds, P25 and α-Fe_2O_3/ZnO heterostructures.

the intensity of the peaks of 554 nm decreased gradually, suggesting that the RhB was gradually photodegraded by the iron oxide/ZnO core−shell heterostructures. And the photographs of the color changing of RhB solution (insets in Figure 7a, b) clear reveal that the RhB have been degraded. The as-used α-Fe_2O_3 seeds and commercial TiO_2 nanoparticles (P25, Degussa) were used as received for comparison purpose in this experiment. In general, the photodegradation of RhB catalyzed by the semiconductor nanomaterials follows a first-order rate law,[20,21] $-\ln(C/C_0) = Kt$, where K is the apparent rate constant of the degradation. Figure 7c shows the effect of different samples on the kinetics of RhB. In our experiment, K was found to be 0. 856% min^{-1}, 1.53% min^{-1}, and 2.40% min^{-1} for the as-obtained α-Fe_2O_3/ZnO core−shell samples of S1, S2 and S3, respectively. Moreover, the K values were found to be 0.341% min^{-1} and 1.13% min^{-1} for the α-Fe_2O_3 seeds and P25, respectively. The current K value is higher than the other reports of zinc oxide nanomaterials were using to photodegrade

dx.doi.org/10.1021/am300669a | ACS Appl. Mater. Interfaces 2012, 4, 3602−3609

the RhB, such as ZnO nanotetrapods,[22] Co^{2+} ions-doped ZnO nanorods,[23] CeO_2–ZnO composite nanofibers,[24] TiO_2/ZnO composite nanofibers,[25] etc. Figure 7d displays the degradability of different samples, and the α-Fe_2O_3/ZnO core–shell nanoparticles display clear enhanced photodegradation ability. Such improvement can be attributed to the several outstanding features of the iron oxide/ZnO core–shell heterostructures, including the small size of the semiconductor clusters and mesoporous morphology, high surface volume ratio, and effective electron–hole separation of the Schottky barriers.[26]

As we have known, ZnO has no absorption response to the visible light due to its wide band gap, thus, the light absorption of α-Fe_2O_3/ZnO core–shell heterostructures was solely contributed by the α-Fe_2O_3 component in the photocatalysis experiments (as shown the UV–vis spectra of α-Fe_2O_3 seeds and α-Fe_2O_3/ZnO samples in Figure S4 in the Supporting Information). Obviously, the composites contain less α-Fe_2O_3 than the pure seeds with same weight. However, all of composite particles exhibited better-enhanced photocatalytic efficiency than the pure α-Fe_2O_3 seeds, which must be correlated to the complex band configuration of the α-Fe_2O_3/ZnO core–shell heterostructures. The improvement is a result of the confined potential of the excited electron–hole pair, which reduces their interaction with traps on the surface and the environment. As shown in Figure 8, the band configuration

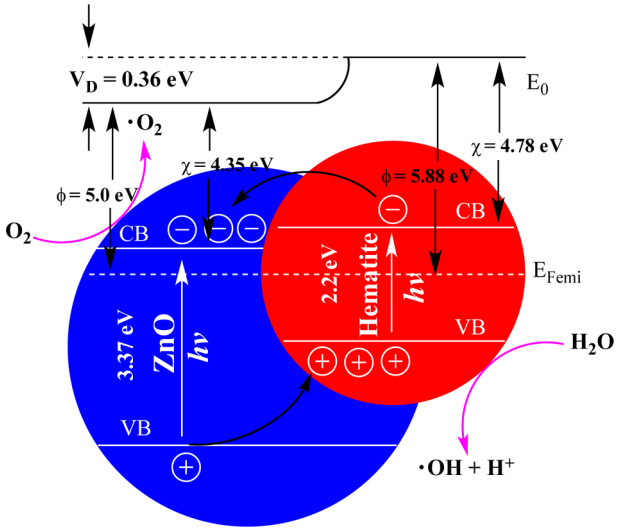

Figure 8. Schematic diagram showing band configuration and electron–hole separation at interface of α-Fe_2O_3/ZnO composite nanospindles under light irradiation; χ is the electron affinity, ϕ is the work function, V_D the contact potential, E_0 the vacuum level, E_{Femi} denotes Fermi level of α-Fe_2O_3/ZnO core–shell structures.

and electron–hole separation at interface of α-Fe_2O_3/ZnO composite nanospindles under light irradiation is proposed. Under UV and visible light irradiation, the photogenerated electrons in conduction band (CB) of α-Fe_2O_3 core tended to transfer to that the CB of ZnO due to the driving by the decreased potential energy. This core–shell heterostructure can reduce the electron–hole recombination probability and enable to increase the electron mobility, and the photogenerated electrons and holes would separate at the α-Fe_2O_3/ZnO interface.[27] Consequently, the electrons and holes were transferred to the surfaces of α-Fe_2O_3 and ZnO, respectively, and finally formed as hydroxyl radicals (·OH). And the superoxygen radicals ($\cdot O_2$) would be formed by the combination of electrons with O_2 adsorbed on the surface of ZnO. As a powerful oxidant, the hydroxyl radicals could decompose effectively the organic pollutes such as RhB. However, the photocatalytic mechanism of these fabricated semiconductor nanostructures is very complicated.[28−30] We will further do a series of experiments focusing on the influence of the different batches of iron oxides/ZnO samples on photocatalytic activity and do extended research on the degradation mechanism influenced by the morphology and nanostructure of iron oxide/ZnO core–shell heterostructures.

CONCLUSION

In summary, the α-Fe_2O_3/ZnO core–shell nanostructures have been successfully fabricated by a facile three-step strategy. The material composition and stoichiometry, as well as these magnetic and optical properties, have been examined and verified by various characterization techniques, the thickness of ZnO layer can be simply tailored by the concentration of zinc precursor. The α-Fe_2O_3/ZnO core–shell nanostructures have been investigated for photocatalysis applications. The results show that the photocatalytic degradation abilities of the spindlelike α-Fe_2O_3 nanoparticles can be significantly enhanced by the ZnO shell coating for RhB dyes, mainly because of the effective electron–hole separation at the interfaces of the core–shell heterostructures. Significantly, the enhanced performance demonstrates the importance of evaluating new composite photocatalysts, and the core–shell nanostructure reported in this work provides a new path to fabricate heterostructural materials for photocatalytical applications.

ASSOCIATED CONTENT

Supporting Information

XRD patterns for before and after annealing treatment of hematite seeds (Figure S1), nitrogen adsorption–desorption isotherms of sample S2 (Figure S2), HRTEM images of hematite seeds (Figure S3), and UV–vis absorption spectra of hematite and hematite/ZnO samples (Figure S4). This material is available free of charge via the Internet at http://pubs.acs.org.

AUTHOR INFORMATION

Corresponding Author

*Tel: +86-27-68752567. Fax: +86-27-68753587. E-mail: weiwu@whu.edu.cn (W.W.); czjiang@whu.edu.cn (C.J.).

Notes

The authors declare no competing financial interest.

ACKNOWLEDGMENTS

The author thanks the NSFC (10905043, 11005082, 91026014, 11175133, 51171132), the Foundations from Chinese Ministry of Education (311003, 20100141120042, 20110141130004), China Postdoctoral Science Foundation (2012M511661), Young Chenguang Project of Wuhan City (201050231055), and the Fundamental Research Funds for the Central Universities, Hubei Provincial Natural Science Foundation (2011CDB270).

REFERENCES

(1) Wu, W.; He, Q. G.; Jiang, C. Z. *Nanoscale Res. Lett.* **2008**, *3* (11), 397–415.
(2) Vinu, R.; Madras, G. *J. Indian Inst. Sci.* **2010**, *90* (2), 189–230.

(3) Chu, D.; Masuda, Y.; Ohji, T.; Kato, K. *Langmuir* **2009**, *26* (4), 2811−2815.
(4) Wang, J.; Jing, L. Q.; Xue, L. P.; Qu, Y. C.; Fu, H. G. *J. Hazard. Mater.* **2008**, *160* (1), 208−212.
(5) Wu, W.; Zhang, S. F.; Ren, F.; Xiao, X. H.; Zhou, J.; Jiang, C. Z. *Nanoscale* **2011**, *3* (11), 4676−4684.
(6) Wu, W.; Xiao, X. H.; Zhang, S. F.; Ren, F.; Jiang, C. Z. *Nanoscale Res. Lett.* **2011**, *6* (1), 533.
(7) Chiu, W.; Khiew, P.; Cloke, M.; Isa, D.; Lim, H.; Tan, T.; Huang, N.; Radiman, S.; Abd-Shukor, R.; Hamid, M. A. A.; Chia, C. *J. Phys. Chem. C* **2010**, *114* (18), 8212−8218.
(8) Chen, Y.-J.; Zhang, F.; Zhao, G.-g.; Fang, X.-y.; Jin, H.-B.; Gao, P.; Zhu, C.-L.; Cao, M.-S.; Xiao, G. *J. Phys. Chem. C* **2010**, *114* (20), 9239−9244.
(9) Zhang, S.; Wu, W.; Xiao, X.; Zhou, J.; Ren, F.; Jiang, C. *Nanoscale Res. Lett.* **2011**, *6* (1), 89.
(10) Bharathi, S.; Nataraj, D.; Mangalaraj, D.; Masuda, Y.; Senthil, K.; Yong, K. *J. Phys. D: Appl. Phys.* **2010**, *43* (1), 015501.
(11) Zhou, Z.; Tian, S.; Zeng, D.; Tang, G.; Xie, C. *J. Alloys Compd.* **2012**, *513* (0), 213−219.
(12) Chiu, W.; Khiew, P.; Cloke, M.; Isa, D.; Lim, H.; Tan, T.; Huang, N.; Radiman, S.; Abd-Shukor, R.; Hamid, M. A. A.; Chia, C. H. *J. Phys. Chem. C* **2010**, *114* (18), 8212−8218.
(13) Zhou, T.; Lu, M.; Zhang, Z.; Gong, H.; Chin, W. S.; Liu, B. *Adv. Mater.* **2010**, *22* (3), 403−406.
(14) Wu, W.; Xiao, X. H.; Peng, T. C.; Jiang, C. Z. *Chem.−Asian J.* **2010**, *5* (2), 315−321.
(15) Wu, W.; He, Q. G.; Chen, H.; Tang, J. X.; Nie, L. B. *Nanotechnology* **2007**, *18* (14), 145609.
(16) Zhu, Y. F.; Kockrick, E.; Ikoma, T.; Hanagata, N.; Kaskel, S. *Chem. Mater.* **2009**, *21* (12), 2547−2553.
(17) Zeng, H.; Li, J.; Wang, Z. L.; Liu, J. P.; Sun, S. H. *Nano Lett.* **2004**, *4* (1), 187−190.
(18) Gupta, R. K.; Ghosh, K.; Dong, L.; Kahol, P. K. *Physica E* **2011**, *43* (5), 1095−1098.
(19) Zysler, R. D.; Fiorani, D.; Testa, A. M.; Suber, L.; Agostinelli, E.; Godinho, M. *Phys. Rev. B* **2003**, *68* (21), 212408.
(20) Wang, G.; Lu, W.; Li, J. H.; Choi, J.; Jeong, Y. S.; Choi, S. Y.; Park, J. B.; Ryu, M. K.; Lee, K. *Small* **2006**, *2* (12), 1436−1439.
(21) Liu, Z. Y.; Sun, D. D. L.; Guo, P.; Leckie, J. O. *Nano Lett.* **2007**, *7* (4), 1081−1085.
(22) Wan, Q.; Wang, T. H.; Zhao, J. C. *Appl. Phys. Lett.* **2005**, *87* (8), 083105.
(23) Qiu, X. Q.; Li, G. S.; Sun, X. F.; Li, L. P.; Fu, X. Z. *Nanotechnology* **2008**, *19* (21), 215703.
(24) Li, C.; Chen, R.; Zhang, X.; Shu, S.; Xiong, J.; Zheng, Y.; Dong, W. *Mater. Lett.* **2011**, *65* (9), 1327−1330.
(25) Liu, R. L.; Ye, H. Y.; Xiong, X. P.; Liu, H. Q. *Mater. Chem. Phys.* **2010**, *121* (3), 432−439.
(26) Zeng, H. B.; Cai, W. P.; Liu, P. S.; Xu, X. X.; Zhou, H. J.; Klingshirn, C.; Kalt, H. *Acs Nano* **2008**, *2* (8), 1661−1670.
(27) Niu, M. T.; Huang, F.; Cui, L. F.; Huang, P.; Yu, Y. L.; Wang, Y. S. *ACS Nano* **2010**, *4* (2), 681−688.
(28) Byrappa, K.; Subramani, A. K.; Ananda, S.; Rai, K. M. L.; Dinesh, R.; Yoshimura, M. *Bull. Mater. Sci.* **2006**, *29* (5), 433−438.
(29) Hu, Y.; Liu, Y.; Qian, H.; Li, Z.; Chen, J. *Langmuir* **2010**, *26* (23), 18570−18575.
(30) Wu, W.; Zhang, S. F.; Zhou, J.; Xiao, X. H.; Ren, F.; Jiang, C. Z. *Chem.—Eur. J.* **2011**, *17* (35), 9708−9719.